

## Article

# Overcome the Energy Gap Law in Near-Infrared Emissive Aggregates via Nonadiabatic Coupling Suppression

Jie Xue,<sup>1,2</sup> Jingyi Xu,<sup>1</sup> Jiajun Ren,<sup>1,\*</sup> Qingxin Liang,<sup>1</sup> Qi Ou,<sup>1</sup> Rui Wang,<sup>1</sup> Zhigang Shuai,<sup>1</sup> and Juan Qiao<sup>1,2,3,\*\*</sup>

<sup>1</sup>Key Lab of Organic Optoelectronics and Molecular Engineering of Ministry of Education, Department of Chemistry, Tsinghua University, Beijing, 100084, P. R. China

<sup>2</sup>Center for Flexible Electronics Technology, Tsinghua University, Beijing 100084, P. R. China

<sup>3</sup>Lead Contact

\*Correspondence: [renjj@tsinghua.edu.cn](mailto:renjj@tsinghua.edu.cn)

\*\*Correspondence: [qjuan@mail.tsinghua.edu.cn](mailto:qjuan@mail.tsinghua.edu.cn)

## ABSTRACT

The pursuing of purely organic materials with high-efficiency near-infrared (NIR) emissions is fundamentally limited by the large non-radiative decay rates ( $k_{nr}$ ) governed by the energy gap law. Here, we demonstrated a feasible and innovative strategy by employing intermolecular charge-transfer (CT) aggregates (CTA) to realize high-efficiency NIR emissions via nonadiabatic coupling suppression. The formation of CTA engenders intermolecular CT in the excited states; thereby, not only reducing the electronic nonadiabatic coupling and contributing to small  $k_{nr}$  for high-efficiency NIR photoluminescence, but also stabilizing excited-state energies and achieving thermally activated delayed fluorescence for high-efficiency NIR electroluminescence. This work provides new insights into aggregates and opens a new avenue for organic materials to overcome the energy gap law and achieve high-efficiency NIR emissions.

Nonadiabatic coupling, intermolecular charge-transfer, near-infrared, molecular aggregates, organic light-emitting diodes, thermally activated delayed fluorescence

## INTRODUCTION

Harnessing the near-infrared (NIR) light is of great importance for optogenetics, phototherapy, bio-imaging, medical diagnosis and optical communications.<sup>1-5</sup> In recent years, NIR organic materials have attracted rapidly growing interest because of their potential as efficient, low-toxicity, low-cost and even disposable NIR photosensitizer and light sources.<sup>3-4</sup> Particularly, the inherent flexibility of organic materials has accelerated the development of NIR organic light-emitting diodes (OLEDs) as flexible, wearable and implantable devices.<sup>4-9</sup> Extending  $\pi$ -conjugation length and employing donor-acceptor charge transfer state have proven to be effective molecular design strategies to realize NIR emissions.<sup>3</sup> However, these conventional NIR organic molecules usually suffer from large non-radiative decay rates ( $k_{nr}$ ) and low photoluminescence (PL) quantum yields (PLQY) due to the energy gap law,<sup>4, 10-11</sup> which dictates accelerated non-radiative processes from the lowest excited state ( $S_1$ ) to ground state ( $S_0$ ) caused by molecular vibrations as the optical energy gap falls towards deep-red and NIR region. Therefore, high-efficiency NIR-OLEDs are still rare, even though great breakthroughs have been made for purely organic materials to harvest the weakly emissive triplet excitons generated by electroexcitation.<sup>12-15</sup>

## The bigger picture

Overcome the energy gap law! Invisible near-infrared (NIR) light plays a highly visible role in biomedical sciences, photovoltaics and optical communications, benefiting human life. Though urgently needed for flexible, wearable and implantable applications, NIR organic materials suffer from accelerated non-radiative decay rates ( $k_{nr}$ ) and the resulted poor luminous efficiency as governed by the energy gap law. To date, reported endeavors to decelerate  $k_{nr}$  are mainly focusing on reducing the electron-vibration coupling with the electronic nonadiabatic coupling (NAC) assumed as a constant. Here, we uncover that the suppression of NAC is a novel approach to decelerate  $k_{nr}$  and overcome the energy gap law. Also, a feasible strategy was demonstrated by forming intermolecular charge-transfer aggregates (CTA) to suppress NAC and thus achieve high-efficiency NIR emission. This work provides a new avenue for organic materials to overcome the energy gap law.

To alleviate the limitation imposed by the energy gap law, considerable efforts have been made for organic materials to decelerate the non-radiative decay processes by reducing the electron-vibration coupling. At single-molecule level, employing rigid molecular structure can hinder low-frequency vibrations in molecules, and perdeuterated or perfluorinated approaches can alleviate high-frequency vibrations.<sup>16-18</sup> Nevertheless, those strategies would inevitably increase the difficulty and cost of synthesis. Beyond the single-molecule level, advances in understanding the aggregation effect on organic luminescence indicate that intermolecular packing sometimes can hinder the non-radiative decay processes caused by low-frequency vibrations of functional groups.<sup>19-20</sup> However, there is still a large room for the improvement of the luminescence efficiency of NIR organic materials, which requires deeper insights into the energy gap law.

In this work, from a fundamental perspective on the energy gap law, we found the suppression of electronic nonadiabatic coupling is a novel approach for organic emissive materials to decelerate the non-radiative decay processes and overcome the energy gap law. Furthermore, we demonstrated a feasible strategy by employing intermolecular charge-transfer (CT) aggregates (CTA) to suppress the nonadiabatic coupling and achieve high-efficiency NIR emissions. The formation of CTA with the involvement of intermolecular CT (xCT) in the excited states can not only reduce the nonadiabatic coupling, which leads to a small  $k_{nr}$  for high-efficiency NIR photoluminescence, but also stabilize excited-state energies, which induces strong thermally activated delayed fluorescence (TADF) for high-efficiency NIR electroluminescence (EL). The developed purely organic CTA emitter exhibited widely-tunable emissions from 621 to 802 nm with high PLQYs of over 80% in NIR region and high maximum external quantum efficiencies (EQEs) of 17.0% in NIR-OLEDs.

## RESULTS

### Theoretical Analysis and Conceptual Design

First, we briefly review the theoretical background of the non-radiative decay rate  $k_{nr}$ . For organic molecules in the weak coupling limit (Huang-Rhys factor  $S_i \ll 1$ ),  $k_{nr}$  can be expressed as<sup>11</sup>

$$k_{nr} = \sum_l C_l^2 \frac{\sqrt{2\pi}}{\omega_M \Delta E} \exp\{-\sum_i S_i\} \exp\left\{-\frac{\Delta E}{\omega_M} \left[\ln\left(\frac{\Delta E}{\lambda_M}\right) - 1\right]\right\} \quad (\text{Equation 1})$$

The prefactor  $C_l^2$  is related to the nonadiabatic coupling elements (NACE) between the ground state  $\varphi_{gs}$  and the excited state  $\varphi_{ex}$  along mode  $l$ , which is called the promoting mode triggering the electronic transition.

$$C_l^2 = \left| \left\langle \varphi_{ex} \left| \frac{\partial}{\partial q_l} \right| \varphi_{gs} \right\rangle \right|^2 \frac{\omega_l}{2} \quad (\text{Equation 2})$$

The other parts of Eq. (1) are related to the Franck-Condon factor weighted density of states — the overlap between the initial and final vibrational wavefunctions, which represents the ability of vibrations to receive the electronic energy.  $\omega_M$  is the frequency of the normal vibrations of maximum frequency.  $\lambda_M$  is the total reorganization energy of the vibrations with frequency  $\omega_M$ .  $\Delta E$  is the adiabatic energy gap between the electronic ground and excited states. Commonly, it is believed that  $k_{nr}$  would increase exponentially with the decrease of  $\Delta E$  under the assumption that the prefactor  $C_l^2$  is unchanged. This is the widely known energy gap law and mainly hinders the development of high-efficiency NIR materials.

From Eq. (1), it is clear that the  $k_{nr}$  of organic molecules are determined by two factors, the electronic nonadiabatic coupling and the Franck-Condon factor weighted density of states. To date, strategies for organic materials to reduce  $k_{nr}$  are mainly focusing on suppressing the second part of Eq. (1) by reducing  $\lambda_M$  and  $\omega_M$ .<sup>16-22</sup> Notably, Zhou and Chi *et al.* proposed that exciton delocalization in well-aligned Pt(II) complexes can reduce the reorganization energy  $\lambda_M$  and achieve high-efficiency NIR-OLEDs.<sup>22</sup> Besides the suppression of electron-vibration coupling, the reduction of electronic nonadiabatic coupling is another approach to reduce  $k_{nr}$  and overcome the energy gap law. However, the prefactor  $C_l^2$  corresponding to the electronic NACE is commonly assumed as a constant and its effect is rarely discussed. Within the complete basis set limit,<sup>23</sup> the NACE is qualitatively proportional to the electronic transition density, determined by the overlap between the electron and hole wavefunction as shown in Eqs. (3) and (4).

$$\left\langle \varphi_{ex} \left| \frac{\partial}{\partial q_l} \right| \varphi_{gs} \right\rangle \approx \frac{1}{E_{ex} - E_{gs}} \sum_{\sigma} \frac{Z_{\sigma} e^2}{\sqrt{M_{\sigma}}} \sum_{i=x,y,z} E_{\sigma i} L_{\sigma i, l} \quad (\text{Equation 3})$$

$$E_{\sigma i} = \int d\vec{r} \rho(\vec{r}) \frac{e(r_i - R_{\sigma i})}{|\vec{r} - \vec{R}_{\sigma}|^3} \approx \int d\vec{r} \phi_{elec}(\vec{r}) \phi_{hole}(\vec{r}) \frac{e(r_i - R_{\sigma i})}{|\vec{r} - \vec{R}_{\sigma}|^3} \quad (\text{Equation 4})$$

where  $L_{\sigma i,l}$  is the transformation matrix between the normal coordinates and Cartesian coordinates and  $E_{\sigma i}$  is atomic electric field experienced by the overlap of electron and hole from the excited state. From Eqs. (1)–(4), we propose that the decrease of the overlap of electron and hole in the excited states can reduce the prefactor  $C_l^2$ , thus suppressing the non-radiative decay processes for a small  $k_{nr}$ . Interestingly, this coincides with the design strategy of TADF materials, which needs to minimize the energy gaps ( $\Delta E_{ST}$ ) between the  $S_1$  and lowest triplet ( $T_1$ ) excited states by decreasing the overlap of electron and hole of the excited states.

### Molecular Design and Synthesis

Recently, we found the formation of J-aggregates with strong xCT can significantly stabilize the excited-state energies of organic materials, thus inducing and enhancing highly efficient TADF.<sup>24</sup> Most importantly, the formation of such molecular aggregates can lead to a decreased  $k_{nr}$  with the decrease of the optical energy gap, totally deviating from the exponential increase trend imposed by the energy gap law.<sup>24</sup> Although the underlying mechanism was unclear at that time, it could benefit from the nonadiabatic coupling suppression induced by xCT with the larger separation of electron and hole than that of intramolecular CT (iCT). To illustrate the underlying mechanism and achieve high-efficiency NIR emissions, the molecule dpTPAAP (Figure 1) for CTA was designed based on the reported TPAAP with the same electron acceptor acenaphtho[1,2-*b*]pyrazine-8,9-dicarbonitrile (AP) and modified electron donor bis(biphenyl-4-yl)phenylamine (dpTPA).<sup>24</sup> The addition of phenyl groups could increase the delocalization of the highest occupied molecular orbital (HOMO), which would be conducive to red-shifted emission with high PLQY.<sup>25-26</sup> And the similar donor-acceptor framework could endow dpTPAAP with strong xCT in aggregation states to construct CTA for NIR emission. For comparison, an iCT molecule with similar molecular framework, dpTPAAZ was designed by fusing electron acceptor pyrazine on the acceptor moiety of dpTPAAP to enhance the iCT and realize NIR emission in single molecule. The fusion of rigid pyrazine could maintain the molecular rigidity, thus reducing the extra non-radiative decay processes as much as possible. The comparative investigations on photophysical behaviors of CTA and commonly-used iCT molecules were conducted to uncover the distinct underlying mechanism and explore the rational design of high-efficiency NIR organic materials.

Both dpTPAAP and dpTPAAZ were synthesized in three steps involving bromination, Suzuki-Miyaura cross-coupling reaction and dehydration cyclization reaction. These new compounds were characterized by NMR spectroscopy, high-resolution mass spectrometry, and elemental analysis. Thermogravimetric analysis (TGA) measurements revealed that both dpTPAAP and dpTPAAZ have high decomposition temperatures ( $T_d$ , corresponding to 5% weight loss) at 414 and 498 °C, respectively.

### Single Crystal and Molecular Packing

During temperature gradient vacuum sublimation, single crystals of dpTPAAP were readily obtained. The molecular structure and packing motifs of dpTPAAP in crystalline states were identified by single-crystal X-ray crystallographic analysis. The dpTPAAP molecules possess relatively planar structures and the dihedral angle between donor and acceptor subunits is 33° (Figure 2A). In crystalline state, the nearest neighbouring dpTPAAP molecules form dimers in a face-to-face fashion (Figure 2B) with the donor of one molecule close to the acceptor of the other molecule, which are supported by intermolecular CN...H-C interactions with a distance of 2.886 Å and intermolecular  $\pi$ ... $\pi$  interactions with a distance of 3.521 Å between the AP acceptor cores. These head-to-tail dimers pack up in a herringbone arrangement in the crystal (Figure 2C), which is much different from the staircase packing mode of its counterpart TPAAP.<sup>24</sup>

### Photophysical Properties

To study the photophysical properties of these compounds as single molecules, oxygen-free dilute toluene solutions ( $1 \times 10^{-5}$  mol L<sup>-1</sup>) of dpTPAAP and dpTPAAZ were prepared. As shown in Figure 3A, the intense absorption bands below 430 nm are assigned to the localized  $\pi$ - $\pi^*$  transitions and the moderate absorption bands over 430 nm are ascribed to the iCT transitions. The broad iCT absorption band of dpTPAAZ can be deconvoluted (Gaussian multi-peak fitting) into two absorption bands (Figure S2); the high-energy band with peak at 466 nm corresponds to the second lowest excited single state ( $S_2$ ), and the low-energy band with peak at 538 nm corresponds to  $S_1$ , which is red-shifted compared with that of dpTPAAP

with the peak at 501 nm due to the enhancement of iCT. Under photoexcitation, dpTPAAP displays intense red fluorescence ( $\lambda_{\text{max}} = 624$  nm) with a high PLQY of up to 97.4% and a short lifetime of 7.94 ns (Figure S3). The remarkable PLQY results from high  $k_r$  value of  $1.2 \times 10^8 \text{ s}^{-1}$  and low  $k_{\text{nr}}$  value of  $3.3 \times 10^6 \text{ s}^{-1}$ . As expected, thanks to the enhancement of iCT, dpTPAAZ exhibits largely red-shifted emission into desired NIR region ( $\lambda_{\text{max}} = 763$  nm) in toluene solution. Unfortunately, such large red-shift of emission leads to a dramatically reduced PLQY to 7.6%. The low PLQY of dpTPAAZ results from the low  $k_r$  value of  $1.8 \times 10^7 \text{ s}^{-1}$  and high  $k_{\text{nr}}$  value of  $2.2 \times 10^8 \text{ s}^{-1}$ . In comparison with dpTPAAP, dpTPAAZ showed almost one order of magnitude smaller  $k_r$  value and two order of magnitude larger  $k_{\text{nr}}$  value, clearly manifesting that the photophysical behaviours of single organic molecule is severely limited by the energy gap law.

In addition to enhancing iCT at the level of single molecule, the formation of aggregates with strong xCT could also achieve desired red-shift of emission.<sup>24, 27-28</sup> In neat film, dpTPAAP shows desired NIR emission ( $\lambda_{\text{max}} = 802$  nm), with a 178 nm red-shift compared with that in toluene solution. The neat film gives a remarkable PLQY of 13.0%, which is more than three times that of the curcuminoid derivative reported by Adachi et al ( $\lambda_{\text{max}} = 801$  nm and PLQY = 4%).<sup>29</sup> Also, the CT absorption band of the neat film shows a substantial red-shift (~40 nm) with corresponding peak wavelength locating at 541 nm, which indicates the formation of molecular aggregates with strong xCT.<sup>24</sup> The single crystals of dpTPAAP demonstrated further red-shifted absorption and emission ( $\lambda_{\text{max}} = 882$  nm) compared with its neat film (Figure 3A), suggesting a more significant xCT in single crystals. Importantly, dpTPAAP single crystal shows a good PLQY of 4.4%.

To investigate the influences of molecular aggregation and environmental dipole on exciton states of dpTPAAP, we measured the absorption spectra of dpTPAAP in tetrahydrofuran (THF)/water mixtures with different water volume fractions ( $f_w$ ). As shown in Figure 3B, although the polarity of THF/water mixture rises as the increase of  $f_w$  from 0% to 50%, the absorption spectra of dpTPAAP is almost unchanged, thus excluding the possibility of environmental dipole induced large red-shift of absorption. The further increase of  $f_w$  from 50% leads to an abrupt red-shift of CT absorption band accompanied by the formation of nanoparticles with the peak finally pinned at 532 nm, manifesting that the formation of molecular aggregates is the main cause for the large red-shift of CT absorption band, which greatly stabilizes the exciton states.

To explore the evolution of molecular aggregates in solid states, we studied the photophysical properties of doped films with dpTPAAP in 2,2',2''-(1,3,5-benzinetriyl)-tris(1-phenyl-1-H-benzimidazole) (TPBi) at different doping concentrations. As shown in Figure 3C, the absorption spectra of doped films show progressive red-shift with increasing doping concentration, manifesting the gradual formation of molecular aggregates. Meanwhile, these films demonstrate widely-tunable PL by simply controlling the doping concentration (Figure 3D and 3E). At very low doping concentration of 0.1 wt%, the doped film displays strong red PL ( $\lambda_{\text{max}} = 621$  nm), which is similar to the PL of dpTPAAP in dilute toluene solutions. As the increase of doping concentration, 0.5 wt% and 1 wt% doped film give strong deep-red (DR) emissions at 653 nm and 677 nm with very high PLQYs of 92.1% and 89.4%, respectively. When doping concentration increases to 5 wt%, the doped film displays desired NIR emission ( $\lambda_{\text{max}} = 707$  nm) with a high PLQY of 82.2%. The doped films show persistently red-shifted PL as the doping concentration continuously increases.

Notably, the 30 wt% doped film realizes the desired NIR PL with peak wavelength at 760 nm, which is almost the same to the PL ( $\lambda_{\text{max}} = 763$  nm) of dpTPAAZ molecules in toluene. Moreover, the 30 wt% doped film has an impressive PLQY of up to 38.5%, which is 5 times that of dpTPAAZ molecules in toluene. Such remarkable PLQY benefits from its high  $k_r$  value of  $2.26 \times 10^7 \text{ s}^{-1}$  and low  $k_{\text{nr}}$  value of  $3.60 \times 10^7 \text{ s}^{-1}$ . The  $k_r$  value is 1.2 times that of dpTPAAZ molecules in toluene, which indicates that the formation of such molecular aggregates is favourable to obtain high  $k_r$  values. Importantly, the film displays a substantially reduced  $k_{\text{nr}}$  value by about one order of magnitude compared with that of dpTPAAZ molecules in oxygen-free toluene. This demonstrates that the formation of CTA could significantly suppress the non-radiative decay processes and contribute to a small  $k_{\text{nr}}$  value rather than a rapid increased  $k_{\text{nr}}$  value according to the energy gap law. Meanwhile, the 30 wt% film exhibits prominent TADF consisting of a nanosecond-scale prompt component (average lifetime  $\tau_p = 16.3$  ns) and a microsecond-scale delayed component (average lifetime  $\tau_{\text{TADF}} =$

39.4  $\mu$ s) at room temperature (Figure 3F and Figure S6), which could be ascribed to the substantially reduced  $\Delta E_{ST}$  of only 0.073 eV as the result of molecular aggregation and the self-polarization-induced solid-state solvation effect.<sup>24, 30</sup>

The photophysical properties of dpTPAAZ in the doped films were also studied for comparison. The 5 wt% dpTPAAZ:TPBi film displays NIR emission with peak wavelength at 764 nm (Figure S7) and a low PLQY of 5.9%, which are close to those of dpTPAAZ molecules in toluene ( $\lambda_{max} = 763$  nm, PLQY = 7.6%). From dilute toluene solution to 5 wt% doped film, the  $k_{nr}$  value of dpTPAAZ reduces from  $2.2 \times 10^8$  s<sup>-1</sup> to  $1.4 \times 10^8$  s<sup>-1</sup>, which could be ascribed to the suppression of low-frequency molecular motions in solid state. Remarkably, the 30 wt% dpTPAAP:TPBi film has almost the same emission ( $\lambda_{max} = 760$  nm) to that of the 5 wt% dpTPAAZ:TPBi film, but its  $k_{nr}$  value is only 0.26 times that of the latter. In general, the doped films with high doping concentration would exhibit large  $k_{nr}$  caused by aggregation-caused quenching. The unexpected low  $k_{nr}$  value of 30 wt% dpTPAAP:TPBi film could benefit from the formation of CTA. Consequently, the PLQY of 30 wt% dpTPAAP:TPBi film is 6.5 times that of 5wt% dpTPAAZ:TPBi film.

### Electron Paramagnetic Resonance

To investigate the xCT in the aggregation states, we performed electron paramagnetic resonance (EPR) measurements on the single crystals and neat film of dpTPAAP. As shown in Figure 4A, the single crystals of dpTPAAP under dark condition displayed clear EPR signal with the  $g$ -factor determined to be 2.0033. Under photoexcitation, its EPR signal is slightly enhanced. Unlike the single crystal with long-range order, the neat film of dpTPAAP is more likely to be amorphous (Figure S9). Nevertheless, the neat film of dpTPAAP also displayed EPR signal under dark condition with the  $g$ -factor determined to be 2.0040 (Figure 4B). Under photoexcitation, its EPR signal is remarkably enhanced instead. Both the  $g$ -factors of EPR signals of single crystals and neat film are close to the value of free electron (2.0023), indicating the presence of unpaired electrons. Since dpTPAAP is a closed-shell neutral molecule, the unpaired electrons could be ascribed to the charged ions generated by xCT in the ground state due to the formation of CTA.<sup>27, 31</sup> The significantly enhanced EPR signal of neat film under photoexcitation demonstrates that more charged ions are generated by xCT under photoexcitation, which clearly highlights the xCT nature in the excited states. In comparison, the photoexcitation only led to slightly enhanced EPR signal for dpTPAAP single crystals, which could be ascribed to the opacity of single crystals that allows only a small ratio of molecules photoexcited under illumination.

### Quantum Chemical Calculations

To understand the photophysical behaviours of dpTPAAP, we carried out theoretical investigations on the electronic structures of monomer and dimers in the gas phase using density functional theory (DFT) and time-dependent DFT (TDDFT). An optimal tuning version of  $\omega$ B97XD long-range corrected functional ( $\omega = 0.1264$ ) was used to describe the CT excited states.<sup>32</sup> The  $S_1$  and  $T_1$  energies of the monomer at the optimized  $S_0$  geometry were calculated to be 2.89 eV and 2.20 eV, respectively. According to the analysis of attachment (electron)/detachment (hole) density and fragment-based transition density matrices (TDM) of  $S_1$  and  $T_1$  state calculated by Q-Chem and Multiwfn 3.7 package,<sup>33-35</sup> the  $S_1$  state of the monomer is predominantly an iCT state from the donor fragment to the acceptor fragment, while the  $T_1$  state is mainly a local excitation state in the acceptor fragment (Figure 5A and 5B).

To investigate the aggregation effect on the electronic structure, we extracted 14 nearest-neighbour dimers from the single crystal (Figure S10). Among them, dimer **1** with a face-to-face stacking leads to the most significant reductions of  $S_1$  and  $T_1$  energies (Table S4), and the  $S_1$  and  $T_1$  energies are 2.31 eV and 1.95 eV respectively at the optimized  $S_0$  geometry. While the  $S_1$  and  $T_1$  energies of other dimer are close to those of monomers. Figure 5C shows that unlike the case of monomer, the  $S_1$  state of dimer **1** is mainly composed of xCT and mixed with a small iCT component. To the contrary,  $T_1$  state maintains the local excitation feature of monomer and is mixed with a small xCT component. This different contributions of xCT component into  $S_1$  and  $T_1$  states result in a different amount of reduction of  $S_1$  and  $T_1$  energies upon aggregation ( $\Delta E_{S_1} = 0.58$  eV,  $\Delta E_{T_1} = 0.25$  eV). Therefore, the singlet-triplet gap decreases in favour of TADF in the solid phase.

Apart from the contribution of xCT, the excitonic coupling is another possible effect to account for the aggregation induced spectrum shift. After Boys-localized diabaticization carried out in the developmental version of Q-Chem within the lowest 4 singlet excited states (Figure 5D), it is clear to see that they are composed of 2 degenerate low-energy pure xCT states and 2 degenerate high-energy pure iCT states. The large electronic coupling  $\langle \text{xCT}_1 | H | \text{iCT}_2 \rangle = \langle \text{xCT}_2 | H | \text{iCT}_1 \rangle = -103 \text{ meV}$  may help the weakly emitting xCT state borrow the oscillator strength from the iCT state to enhance  $k_r$  if the ideal degeneracy is broken with static disorder in the real film. However, the excitonic coupling between the iCT states is only 26 meV, which has a minor effect on the  $S_1$  state of dimer **1**.

The introduction of xCT component into the excited states not only reduces the excitation energy, but also reduces NACE, which is essential to the high-efficiency NIR luminescence. In CTA, we found that the reduction of NACE plays a major role in suppressing non-radiative decay process when the  $S_1$  state changes from iCT to xCT upon aggregation. In Figure 6,  $C_l$  in Eq. (1) for different promoting modes of dpTPAAP monomer and dimer **1** are shown. For the monomer, the modes between  $1300 \text{ cm}^{-1}$  and  $1600 \text{ cm}^{-1}$ , typically corresponding to the high-frequency stretching vibrations of skeleton bonds, contribute most to the prefactor. In contrast, for dimer **1**,  $C_l$  in the same frequency window is largely suppressed. The largest component decreases from  $40 \text{ cm}^{-1}$  to  $15 \text{ cm}^{-1}$ . This reduction is due to that the NACE is qualitatively proportional to the overlap between the hole and electron wavefunction as shown in Eq. (4). Though we only consider the minimal dimer model in our calculation, we expect that in the thin film, aggregates larger than the dimer will further delocalize the wavefunction of hole and electron and lead to a smaller NACE. The reduction of the prefactor  $C_l^2$  will partially compensate for the increase in  $k_{nr}$  induced by the reduction in energy gap. It could account for the much smaller  $k_{nr}$  of CTA compared with that of iCT molecules with similar emission wavelength and molecular structure, and could be the underlying mechanism for the observation in the experiments that the  $k_{nr}$  shows even an anti energy gap law behaviour through the formation of molecular aggregates with strong xCT.<sup>24</sup> The similar effect has been discussed in organic solar cells that the electron-hole separation and delocalization in the donor-acceptor interface will reduce the nonadiabatic coupling and hence suppress the non-radiative decay process.<sup>36</sup>

## Device Performance

To evaluate the electroluminescent performance of dpTPAAP, OLEDs were fabricated with multilayer configurations of indium tin oxide (ITO)/1,4,5,8,9,11-hexaazatriphenylenehexacarbonitrile (HATCN, 5 nm, hole-injecting layer)/N,N'-bis(naphthalen-1-yl)-N,N'-bis(phenyl)benzidine (NPB, 70 nm, hole transporting layer)/4,4',4''-tris(carbazol-9-yl)triphenylamine (TCTA, 10 nm, exciton blocking layer)/TPBi: x wt% dpTPAAP (30 nm, emitting layer)/TPBi (60 nm, electron transporting layer)/LiF (1 nm, electron-injecting layer)/Al (150 nm) (device A: x = 1, device B: x = 5, device C: x = 15 and device D: x = 30). As depicted in Figure 7 and Table 1, device A demonstrated intense DR emission with peak wavelength at 675 nm. As the increase of doping concentrations, the EL spectra of devices red-shift and fall into NIR region with peak wavelengths at 710 nm, 730 nm and 752 nm for devices B, C and D, respectively. In addition to the widely-tunable EL by simple doping concentration control, devices A, B, C and D based on dpTPAAP achieved high maximum EQEs of 24.8%, 17.0%, 13.0% and 6.8%, respectively, which may represent the best results for DR and NIR OLEDs based on TADF emitters.<sup>24, 29, 37-41</sup> Importantly, NIR devices B, C and D exhibited high radiant emittances of  $69.06 \text{ W m}^{-2}$ ,  $86.02 \text{ W m}^{-2}$ , and  $78.36 \text{ W m}^{-2}$ , respectively. As the increase of doping concentration, the turn-on voltage decrease from 3.0 V for device A to 2.6 V for device B and to 2.5 V for devices C and D, which could be ascribed to the trap-assisted recombination on the dopants at high doping concentration. In addition, devices with higher doping concentration demonstrate a more rapid increase of current density ( $J$ ) as the increase of voltage, which could be ascribed to the better carrier injection and the formation of percolative charge transport on dopants.<sup>42</sup> As the increase of doping concentration in the emitting layer, devices show alleviated efficiency roll-offs, which could be ascribed to the shortened delayed fluorescence lifetimes for doped films with higher doping concentration,<sup>24</sup> thus reducing the exciton-exciton annihilation and exciton-polaron annihilation at high current density.<sup>43-44</sup> For comparison, Device E based on dpTPAAZ was also fabricated with a configuration of ITO/HATCN (5 nm)/NPB (70 nm)/TCTA (10 nm)/5 wt% dpTPAAZ:TPBi (30 nm)/TPBi (60 nm)/LiF (1 nm)/Al (150 nm). Device E demonstrates NIR emission with peak wavelength at 757 nm, which is close to EL peak of device D based on 30

wt% dpTPAAP:TPBi film. Nevertheless, the maximum EQE of device E is only 1.2% due to the low PLQY of the emitting layer, which is much lower than that of device D. Although with nearly the same emission peak, the much higher EQE of device D than device E suggests the superiority of CTA in achieving high-efficiency NIR EL.

## DISCUSSION

In this contribution, we have presented that the suppression of electronic nonadiabatic coupling is a novel approach for organic emissive materials to suppress the non-radiative decay processes and overcome the energy gap law. Also, a feasible strategy was developed to reduce the electronic nonadiabatic coupling by forming CTA for organic materials to achieve high-efficiency NIR emissions. The developed dpTPAAP molecules, through forming CTA, exhibit widely-tunable emissions from 621 to 802 nm with high PLQYs of over 80% in NIR region. Importantly, in comparison with iCT molecules with similar molecular structure and NIR emission around 760 nm, the CTA emitter displays a 6.5 times higher PLQY contributed by a 3.8 times smaller  $k_{nr}$ . Theoretical investigations reveal that the formation of CTA with the involvement of xCT in the excited states can suppress nonadiabatic coupling, thus alleviating the limitation of energy gap law. The formation of CTA is well verified by the absorption spectra and EPR measurements and rationalized by quantum chemical calculations. The OLEDs fabricated with the CTA emitter exhibited high-efficiency DR and NIR EL. The mechanism illustrated by the theoretical investigations would shed light on the unique photophysical behaviours of xCT emitters and provide a novel approach for organic materials to overcome the energy gap law. It is anticipated that our work paves a superior way for the rational design of high-efficiency NIR organic materials, and lays a foundation for the applications of CTA for a wide variety of fields.

## EXPERIMENTAL PROCEDURES

### Resource availability

#### Lead contact

Further information and requests for resources should be directed to and will be fulfilled by the lead contact, Juan Qiao ([qjuan@mail.tsinghua.edu.cn](mailto:qjuan@mail.tsinghua.edu.cn)).

#### Materials availability

All materials generated in this study are available from the lead contact without restriction

#### Data and code availability

The accession number for the crystal structure CIF reported in this paper is CCDC: 1975023 (dpTPAAP).

### Materials and Synthesis

All reagents and chemicals were reagent grade, commercially available and used without further purification. OLED materials HATCN, NPB, TCTA and TPBi were purchased from Xi'an Polymer Light Technology Corp and were used as received.  $^1\text{H}$  and  $^{13}\text{C}$  NMR spectra were measured on a JEOL ECA 600 spectrometer at ambient temperature. The laser desorption ionization time-of flight mass spectrometry (LDI-TOF-MS) data were obtained using a Shimadzu AXIMA Performance MALDI-TOF instrument in positive detection modes with an applied voltage of 25 kV between the target and the aperture of the time-of-flight analyzer. Elemental analyses were performed on a flash EA 1112 spectrometer.

#### Synthesis of 5-(4-(di([1,1'-biphenyl]-4-yl)amino)phenyl)acenaphthylene-1,2-dione

(4-(di([1,1'-biphenyl]-4-yl)amino)phenyl)boronic acid (2.11 g, 4.8 mmol), 5-Bromoacenaphthylene-1,2-dione (1.04 g, 4mmol),  $\text{K}_2\text{CO}_3$  (1.66 g, 12mmol) and  $\text{Pd}(\text{PPh}_3)_4$  (0.46 g, 0.4mmol) were dissolved in a 100 mL round-bottle flash with 30 mL dioxane and 10 mL deionized water under an argon atmosphere. Then the mixture was stirred under reflux with the temperature of 100°C for 24 hours. After cooling to room temperature, the mixture was poured into 50 mL water and extracted with dichloromethane for three times. The obtained organic layer was washed with water and then dried over  $\text{MgSO}_4$  and concentrated by rotary evaporator. The crude product was purified by column chromatography on silica gel (hexane/dichloromethane = 1:5, v/v) to give 5-(4-(di([1,1'-biphenyl]-4-

yl)amino)phenyl)acenaphthylene-1,2-dione as deep-red solid. Yield: 57%. <sup>1</sup>H NMR (600 MHz, CDCl<sub>3</sub>): δ = 8.50 (dd, *J* = 8.5, 0.8 Hz, 1H), 8.17 (d, *J* = 7.3 Hz, 1H), 8.12 (dd, *J* = 7.0, 0.7 Hz, 1H), 7.86-7.80 (m, 2H), 7.63-7.59 (m, 4H), 7.59-7.56 (m, 4H), 7.54-7.51 (m, 2H), 7.47-7.42 (m, 4H), 7.36-7.29 (m, 8H). HRMS (MALDI-TOF): calcd for C<sub>42</sub>H<sub>27</sub>NO<sub>2</sub> [*M*]<sup>+</sup>: 577.2042, found: 577.2330.

#### *Synthesis of 3-(4-(di([1,1'-biphenyl]-4-yl)amino)phenyl)acenaphtho[1,2-b]pyrazine-8,9-dicarbonitrile (dpTPAAP)*

5-(4-(di([1,1'-biphenyl]-4-yl)amino)phenyl)acenaphthylene-1,2-dione (1.5 g, 2.6 mmol) and diaminomaleonitrile (0.42 g, 3.9 mmol) were dissolved in a 500 mL round-bottle flash with 300 mL glacial acetic acid. Under argon atmosphere, the mixture was stirred under reflux with the temperature of 130 °C for 24 hours. After cooling to room temperature, the mixture was filtered off and washed with acetone, ethanol, water and then dried under vacuum. The crude product was purified by column chromatography on silica gel using hexane/dichloromethane (2:1, v/v) as eluent to give dpTPAAP as dark purple solid. Yield: 84%. This solid was further purified through temperature gradient vacuum sublimation under the temperature of 300-320 °C and atmospheric pressure of 7×10<sup>-4</sup> Pa gave dpTPAAP as a black crystalline solid. <sup>1</sup>H NMR (600 MHz, CDCl<sub>3</sub>): δ = 8.57 (d, *J* = 7.3 Hz, 2H), 8.55 (d, *J* = 8.5 Hz, 1H), 8.00-7.95 (m, 2H), 7.64-7.56 (m, 10H), 7.46 (t, *J* = 7.7 Hz, 4H), 7.40-7.31 (m, 8H). <sup>13</sup>C NMR (150 MHz, CDCl<sub>3</sub>): δ = 154.39, 154.06, 148.47, 146.71, 146.34, 140.41, 136.63, 136.01, 132.23, 131.48, 131.28, 129.92, 129.66, 129.37, 129.19, 128.84, 128.68, 128.17, 127.15, 126.94, 126.77, 126.32, 126.06, 125.25, 122.97, 114.32, 114.28. HRMS (MALDI-TOF): calcd for C<sub>46</sub>H<sub>27</sub>N<sub>5</sub> [*M*]<sup>+</sup>: 649.2266, found: 649.2368. Elemental analysis calcd for C<sub>46</sub>H<sub>27</sub>N<sub>5</sub>: C, 85.03; H, 4.19; N, 10.78. Found: C, 84.85; H, 4.38; N, 10.67.

#### *Synthesis of 3-(4-(di([1,1'-biphenyl]-4-yl)amino)phenyl)acenaphtho[1,2-b]pyrazino[2,3-e]pyrazine-9,10-dicarbonitrile (dpTPAAZ)*

5-(4-(di([1,1'-biphenyl]-4-yl)amino)phenyl)acenaphthylene-1,2-dione (1.5 g, 2.6 mmol) and 5,6-diaminopyrazine-2,3-dicarbonitrile (0.62 g, 3.9 mmol) were dissolved in a 500 mL round-bottle flash with 300 mL glacial acetic acid. Under argon atmosphere, the mixture was stirred under reflux with the temperature of 130 °C for 24 hours. After cooling to room temperature, the mixture was filtered off and washed with acetone, ethanol, water and then dried under vacuum. The crude product was purified by column chromatography on silica gel using hexane/dichloromethane (7:1, v/v) as eluent to give dpTPAAZ as black solid. Yield: 81%. This solid was further purified through temperature gradient vacuum sublimation under the temperature of 360-380 °C and atmospheric pressure of 7×10<sup>-4</sup> Pa gave dpTPAAZ as a black solid. <sup>1</sup>H NMR (600 MHz, CD<sub>2</sub>Cl<sub>2</sub>): δ = 8.77-8.73 (m, 2H), 8.64 (d, *J* = 8.4 Hz, 1H), 8.08-8.04 (m, 2H), 7.68-7.58 (m, 10H), 7.46 (t, *J* = 7.7 Hz, 4H), 7.40-7.31 (m, 8H). <sup>13</sup>C NMR of dpTPAAZ was not obtained because of its low solubility in CDCl<sub>3</sub>. HRMS (MALDI-TOF): calcd for C<sub>48</sub>H<sub>28</sub>N<sub>7</sub><sup>+</sup> [*M*+H]<sup>+</sup>: 701.2401, found: 702.1460. Elemental analysis calcd for C<sub>48</sub>H<sub>27</sub>N<sub>7</sub>: C, 82.15; H, 3.88; N, 13.97. Found: C, 82.06; H, 4.00; N, 13.89.

### Single-crystal Structure

The single crystal of dpTPAAP was obtained in the process of vacuum train sublimation. The low temperature (104.6K) single-crystals X-ray experiments were performed on a Rigaku RAXIS-SPIDER IP diffractometer with graphite-monochromatized MoKα radiation (λ=0.71073 Å). Data collection and reduction, cell refinement, and experiential absorption correction for all compounds were performed with the Rigaku RAPID AUTO software package (Rigaku, 1998, Version 2.30). CCDC 1975023 contain the supplementary crystallographic data for this paper. These data can be obtained free of charge from The Cambridge Crystallographic Data Centre via [www.ccdc.cam.ac.uk/data\\_request/cif](http://www.ccdc.cam.ac.uk/data_request/cif).

### Thermal Properties

Thermogravimetric analyses (TGAs) were performed on a STA 409PC thermogravimeter by measuring the weight loss while heating at a rate of 10 °C min<sup>-1</sup> under nitrogen.

### Electron Paramagnetic Resonance

The EPR measurements were performed on the X-band EPR spectrometer (JEOL, JES FA-200) at room temperature. The EPR measurement under photoexcitation were carried out using a broadband Xe lamp.



### Photophysical Measurement

The  $\Phi_{\text{PL}}$  was measured using an absolute photoluminescence quantum yield measurement system (Hamamatsu C9920-03G) with an excitation wavelength of 390 nm. Absorption spectra of solutions and films were obtained on an Agilent 8453 UV-vis/NIR spectrophotometer and the absorption spectrum of single crystal was obtained on a Hitachi U-3900 UV-vis/NIR spectrophotometer. Emission spectra were collected on an Edinburgh FLS-920 fluorospectrophotometer equipped with a R928P photomultiplier tube with a spectral response range from 200 to 850 nm and a Hamamatsu R5509 photomultiplier tube with response range from 300 to 1700 nm. The fluorescence spectra and phosphorescence spectra used for determining the  $S_1$  and  $T_1$  values were collected on an Edinburgh FLS-920 fluorospectrophotometer with an excitation wavelength of 490 nm. The fluorescence spectra of films were obtained by steady-state photoluminescence measurements at room temperature without time gating, and the phosphorescence spectra of films were recorded by time-gated photoluminescence measurements (delayed by 5 ms) at 77K with a integration time of 5 ms. Transient PL measurements were carried out using a transient spectrometer (Edinburg FLS-920). The prompt parts of transient spectra were collected with a picosecond pulsed Laser (EPL-510,  $\lambda_{\text{ex}} = 505.4$  nm), while the delayed parts of transient spectra were collected with a  $\mu\text{F2}$  microflash lamp ( $\lambda_{\text{ex}} = 505$  nm). The  $1 \times 10^{-5}$  M solution was used for PL spectra measurement. Small-molecule organic films for optical measurements were fabricated by thermal evaporation under high vacuum ( $10^{-4}$  Pa) onto clean quartz substrates.

### Theoretical Calculation

Calculations on the ground and excited electronic states were performed in Gaussian 16 with density functional theory (DFT) and time-dependent DFT (TDDFT) using an optimal tuning version of  $\omega\text{B97XD}$  long-range corrected functional ( $\omega=0.1264$ ) with def2-SVP basis set in gas phase.<sup>32, 45-46</sup> The input files for the hole/electron excitation analysis were prepared by printing orbital pairs with a configuration coefficient  $> 0.001$  using keyword with IOP(9/40 = 3). The diabatization of the electronic states and analysis were performed using Q-Chem and Multiwfn.

### Device Fabrication and Measurements

The devices were fabricated by thermal evaporation under high vacuum (ca.  $4 \times 10^{-4}$  Pa) onto ITO-coated glass substrates. The substrates were carefully cleaned and treated with UV ozone for 10 min before vacuum thermal deposition. All OLED devices were measured in ambient. The voltage, current, luminance and radiant flux characteristics were measured using a Keithley 2400 source meter and an absolute EQE measurement system (Hamamatsu C9920-12 equipped with Hamamatsu PMA-12 Photonic multichannel analyzer C10027-02).

### SUPPLEMENTAL INFORMATION

Supplemental Information includes Supplemental Experimental Procedures, seventeen figures, and four tables, and can be found with this article online.

### ACKNOWLEDGMENTS

This work was supported by the National Key R&D Program of China (Grant No. 2016YFB0401003, No. 2017YFA0204501), National Natural Science Foundation of China (Grant No. 21788102, No. 51773109), National Postdoctoral Program for Innovative Talents (Grant No. BX20180159), and the Project funded by China Postdoctoral Science Foundation (2019M660606).

### AUTHOR CONTRIBUTIONS

J.Xue, J.Xu and Q.L. designed, synthesized and characterized the compounds. J.Xue and J.Xu measured physicochemical properties of materials. J.R. developed the theoretical approach. J.R. and J.Xue performed the computational experiments. Z.S., Q.O. and R.W. participated in the theoretical investigations. J.Xue, J.R. and J.Q. participated in data analysis and wrote the paper. J.Q. supervised the whole work. All authors discussed the results and commented on the manuscript.

### DECLARATION OF INTERESTS

The authors declare no competing interests.

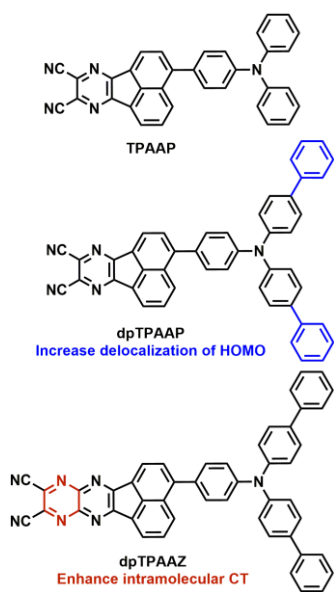


**Figure 1. Molecular design**

Design strategies for organic NIR emitters and chemical structures of dpTPAAP and dpTPAAZ.

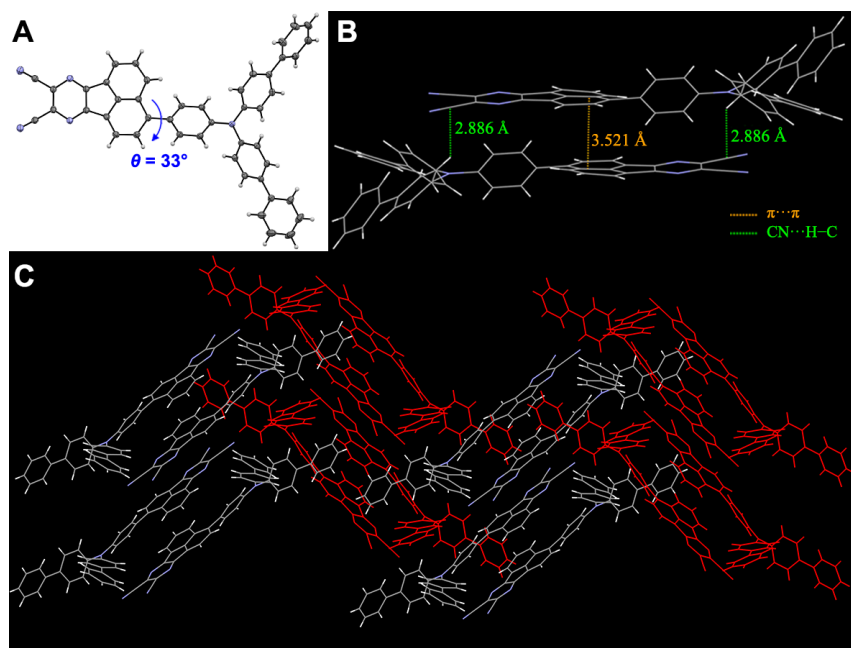


**Figure 2. Single-Crystal Structure**

(A) Single-crystal structure of dpTPAAP with thermal ellipsoids plotted at 50% probability level.

(B) Packing motifs of aggregated dimers.

(C) Packing motifs of dpTPAAP in single crystals.

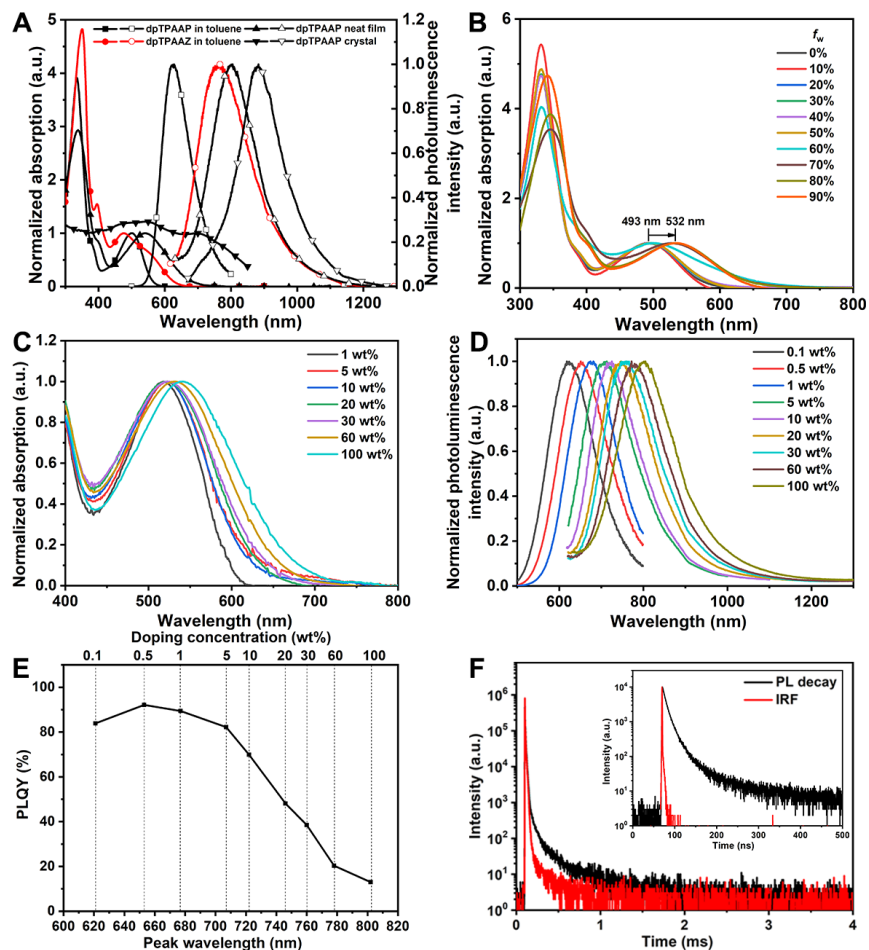


**Figure 3. Photophysical Properties**

(A) Absorption (solid symbol) and PL (open symbol) spectra of dpTPAAP and dpTPAAZ in toluene ( $1 \times 10^{-5}$  mol L $^{-1}$ ), dpTPAAP in neat film and single crystal.

(B) Absorption spectra of dpTPAAP in THF/water mixtures ( $1 \times 10^{-5}$  mol L $^{-1}$ ) with different water fractions ( $f_w$ ).

(C-D) Absorption spectra (C), PL spectra (D) and PLQY (E) of dpTPAAP in solid films with TPBi as host at various doping concentrations at room temperature.

(F) Transient PL decay curves of 30 wt% dpTPAAP:TPBi film. Inset: the prompt decay curves in nanosecond scale.

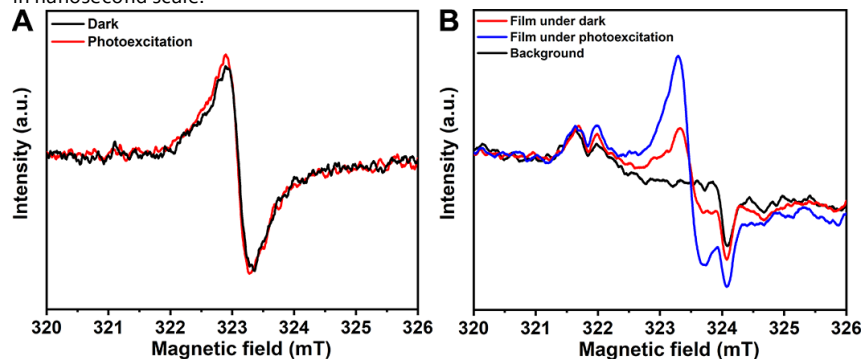


**Figure 4. Electron Paramagnetic Resonance**

(A and B) EPR signals of dpTPAAP single crystals (A) and neat film (B) under dark condition and photoexcitation.

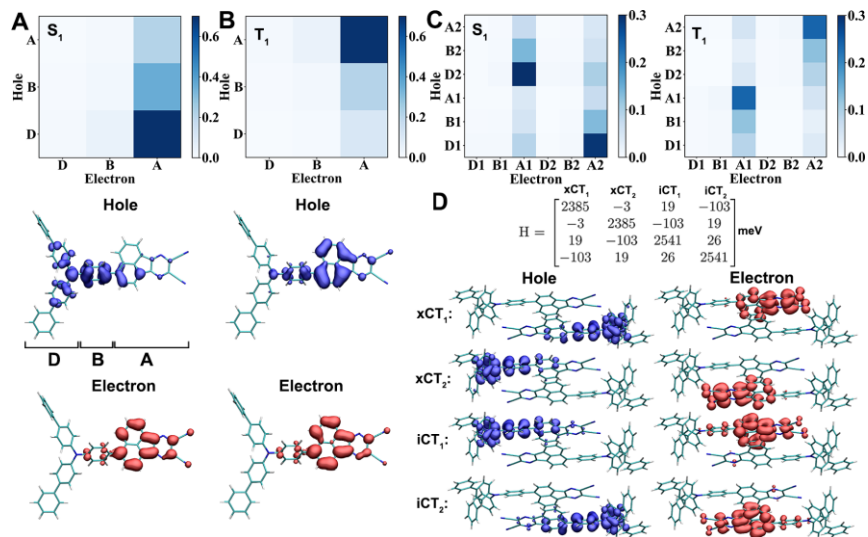


**Figure 5. Quantum chemical calculations**

(A and B) Fragment-based TDM (D/B/A denotes donor/bridge/acceptor) and attachment (electron)/detachment (hole) density (isovalue = 0.001) for (A)  $S_1$  and (B)  $T_1$  state of dpTPAAP monomer.

(C) TDM for  $S_1/T_1$  states of dpTPAAP dimer 1.

(D) The diabatic Hamiltonian and electron/hole density of the lowest 4 diabatic states (2 xCT and 2 iCT) of dpTPAAP dimer 1.

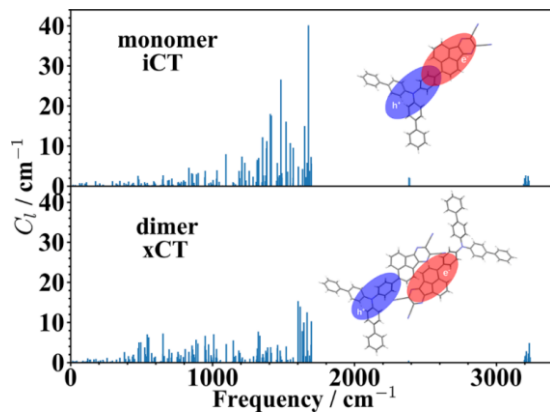


**Figure 6. Nonadiabatic coupling elements**

The prefactor  $C_l$  of  $k_{nr}$  in Eq. (1) for dpTPAAP monomer and dimer 1 at their optimized  $S_0$  structures.

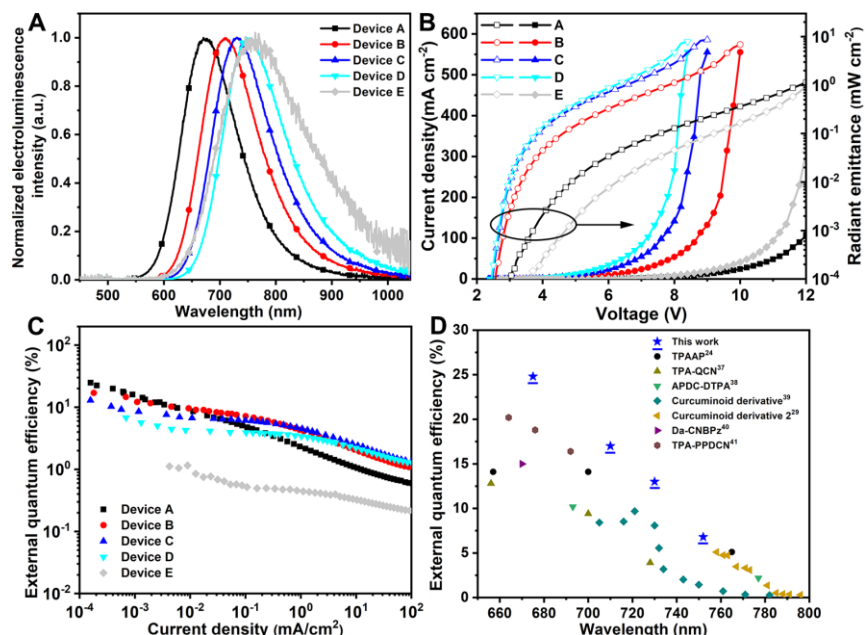


**Figure 7. Device performance of OLEDs**

(A) Electroluminescence spectra recorded at the voltage of  $1 \text{ mA cm}^{-2}$  for devices A, B, C, D and E.

(B) Current density-voltage-radiant emittance characteristics for devices A, B, C, D and E.

(C) EQE as a function of current density.

(D) Maximum EQE summary of the representative deep-red and NIR OLEDs based on TADF emitters with emission peaks from 650 nm to 800 nm.

**Table 1. Electroluminescence characteristics of the devices**

Device	$V_{\text{on}}^a$ (V)	$\lambda_{\text{EL,max}}^b$ (nm)	EQE <sup>c</sup> (%)	Radiant emittance ( $\text{W m}^{-2}$ )
A	3.0	675	24.8/2.3/1.1	11.40 <sup>d</sup>
B	2.6	710	17.0/4.3/2.0	69.06 <sup>e</sup>
C	2.5	730	13.0/4.6/2.5	86.02 <sup>f</sup>
D	2.5	752	6.8/3.4/2.2	78.36 <sup>g</sup>
E	3.6	757	1.2/0.4/0.3	9.44 <sup>d</sup>

<sup>a</sup> $V_{\text{on}}$  is the onset voltage obtained at  $1 \text{ mW m}^{-2}$ .

<sup>b</sup>Recorded at  $1 \text{ mA cm}^{-2}$ .

<sup>c</sup>EQE: maximum, value at  $1 \text{ mA cm}^{-2}$  and value at  $10 \text{ mA cm}^{-2}$ , respectively;

<sup>d</sup>Recorded at 12 V.

<sup>e</sup>Recorded at 10 V.

<sup>f</sup>Recorded at 9 V.

<sup>g</sup>Recorded at 8.4 V.

## REFERENCES

- Bünzli, J.-C. G.; Eliseeva, S. V. (2010). Lanthanide NIR luminescence for telecommunications, bioanalyses and solar energy conversion. *J. Rare Earths* 28, 824-842. 10.1016/S1002-0721(09)60208-8.
- Kerry, Duan, Y.; Liu, B. (2018). Recent Advances of Optical Imaging in the Second Near-Infrared Window. *Adv. Mater.* 30, 1802394. 10.1002/adma.201802394.
- Qian, G.; Wang, Z. Y. (2010). Near-Infrared Organic Compounds and Emerging Applications. *Chem. - Asian J.* 5, 1006-1029. 10.1002/asia.200900596.
- Zampetti, A.; Minotto, A.; Cacialli, F. (2019). Near-Infrared (NIR) Organic Light-Emitting Diodes (OLEDs): Challenges and Opportunities. *Adv. Funct. Mater.* 29, 1807623. 10.1002/adfm.201807623.
- Chen, S.; Weitemier, A. Z.; Zeng, X.; He, L.; Wang, X.; Tao, Y.; Huang, A. J. Y.; Hashimoto, Y.; Kano, M.; Iwasaki, H., et al. (2018). Near-infrared deep brain

- stimulation via upconversion nanoparticle-mediated optogenetics. *Science* 359, 679. 10.1126/science.aag1144.
6. Khan, Y.; Han, D.; Pierre, A.; Ting, J.; Wang, X.; Lochner, C. M.; Bovo, G.; Yaacobi-Gross, N.; Newsome, C.; Wilson, R., et al. (2018). A flexible organic reflectance oximeter array. *Proc. Natl. Acad. Sci. U. S. A.* 115, E11015. 10.1073/pnas.1813053115.
7. Takahiko, Y.; Hajime, N.; Shigeo, H.; Toru, H.; Chihaya, A. (2017). Near-infrared organic light-emitting diodes for biosensing with high operating stability. *Appl. Phys. Express* 10, 074101.
8. Jeon, Y.; Choi, H.-R.; Kwon, J. H.; Choi, S.; Nam, K. M.; Park, K.-C.; Choi, K. C. (2019). Sandwich-structure transferable free-form OLEDs for wearable and disposable skin wound photomedicine. *Light: Sci. Appl.* 8, 114. 10.1038/s41377-019-0221-3. 10.1038/s41377-019-0221-3.
9. Khan, Y.; Han, D.; Ting, J.; Ahmed, M.; Nagisetty, R.; Arias, A. C. (2019). Organic Multi-Channel Optoelectronic Sensors for Wearable Health Monitoring. *IEEE Access* 7, 128114-128124. 10.1109/ACCESS.2019.2939798.
10. Siebrand, W. (1967). Radiationless Transitions in Polyatomic Molecules. I. Calculation of Franck-Condon Factors. *J. Chem. Phys.* 46, 440-447. 10.1063/1.1840685.
11. Englman, R.; Jortner, J. (1970). The energy gap law for radiationless transitions in large molecules. *Mol. Phys.* 18, 145-164. 10.1080/00268977000100171.
12. Yao, L.; Zhang, S.; Wang, R.; Li, W.; Shen, F.; Yang, B.; Ma, Y. (2014). Highly Efficient Near-Infrared Organic Light-Emitting Diode Based on a Butterfly-Shaped Donor-Acceptor Chromophore with Strong Solid-State Fluorescence and a Large Proportion of Radiative Excitons. *Angew. Chem. Int. Ed.* 53, 2119-2123. 10.1002/anie.201308486.
13. Wang, S.; Yan, X.; Cheng, Z.; Zhang, H.; Liu, Y.; Wang, Y. (2015). Highly Efficient Near-Infrared Delayed Fluorescence Organic Light Emitting Diodes Using a Phenanthrene-Based Charge-Transfer Compound. *Angew. Chem. Int. Ed.* 54, 13068-13072. 10.1002/anie.201506687.
14. Peng, Q.; Obolda, A.; Zhang, M.; Li, F. (2015). Organic Light-Emitting Diodes Using a Neutral  $\pi$  Radical as Emitter: The Emission from a Doublet. *Angew. Chem. Int. Ed.* 54, 7091-7095. 10.1002/anie.201500242.
15. Ai, X.; Evans, E. W.; Dong, S.; Gillett, A. J.; Guo, H.; Chen, Y.; Hele, T. J. H.; Friend, R. H.; Li, F. (2018). Efficient radical-based light-emitting diodes with doublet emission. *Nature* 563, 536-540. 10.1038/s41586-018-0695-9.
16. Deng, C.; Niu, Y.; Peng, Q.; Qin, A.; Shuai, Z.; Tang, B. Z. (2011). Theoretical study of radiative and non-radiative decay processes in pyrazine derivatives. *J. Chem. Phys.* 135, 014304. 10.1063/1.3606579.
17. Metcalfe, J.; Phillips, D. (1976). Photophysical processes in fluorinated acetones. *J. Chem. Soc., Faraday Trans. 2* 72, 1574-1583. 10.1039/F29767201574.
18. Siebrand, W.; Williams, D. F. (1968). Radiationless Transitions in Polyatomic Molecules. III. Anharmonicity, Isotope Effects, and Singlet-to-Ground-State Transitions in Aromatic Hydrocarbons. *J. Chem. Phys.* 49, 1860-1871. 10.1063/1.1670318.
19. Yang, J.; Chi, Z.; Zhu, W.; Tang, B. Z.; Li, Z. (2019). Aggregation-induced emission: a coming-of-age ceremony at the age of eighteen. *Sci. China Chem.* 62, 1090-1098. 10.1007/s11426-019-9512-x.
20. Wu, Q.; Deng, C.; Peng, Q.; Niu, Y.; Shuai, Z. (2012). Quantum chemical insights into the aggregation induced emission phenomena: A QM/MM study for pyrazine derivatives. *J. Comput. Chem.* 33, 1862-1869. 10.1002/jcc.23019.
21. Chen, W.-C.; Chou, P.-T.; Cheng, Y.-C. (2019). Low Internal Reorganization Energy of the Metal-Metal-to-Ligand Charge Transfer Emission in Dimeric Pt(II) Complexes. *J. Phys. Chem. C* 123, 10225-10236. 10.1021/acs.jpcc.9b00224.
22. Wei, Y.-C.; Wang, S. F.; Hu, Y.; Liao, L.-S.; Chen, D.-G.; Chang, K.-H.; Wang, C.-W.; Liu, S.-H.; Chan, W.-H.; Liao, J.-L., et al. (2020). Overcoming the energy gap law in near-infrared OLEDs by exciton-vibration decoupling. *Nat. Photonics* 14, 570-577. 10.1038/s41566-020-0653-6.
23. Chernyak, V.; Mukamel, S. (2000). Density-matrix representation of nonadiabatic couplings in time-dependent density functional (TDDFT) theories. *J. Chem. Phys.* 112, 3572-3579. 10.1063/1.480511.
24. Xue, J.; Liang, Q.; Wang, R.; Hou, J.; Li, W.; Peng, Q.; Shuai, Z.; Qiao, J. (2019). Highly Efficient Thermally Activated Delayed Fluorescence via J-Aggregates with Strong Intermolecular Charge Transfer. *Adv. Mater.* 31, 1808242. 10.1002/adma.201808242.
25. Hirata, S.; Sakai, Y.; Masui, K.; Tanaka, H.; Lee, S. Y.; Nomura, H.; Nakamura, N.; Yasumatsu, M.; Nakanotani, H.; Zhang, Q., et al. (2014). Highly efficient blue electroluminescence based on thermally activated delayed fluorescence. *Nat. Mater.* 14, 330. 10.1038/nmat4154.
26. Zhang, Q.; Kuwabara, H.; Potscavage, W. J.; Huang, S.; Hatae, Y.; Shibata, T.; Adachi, C. (2014). Anthraquinone-Based Intramolecular Charge-Transfer Compounds: Computational Molecular Design, Thermally Activated Delayed Fluorescence, and Highly Efficient Red Electroluminescence. *J. Am. Chem. Soc.* 136, 18070-18081. 10.1021/ja510144h.
27. Chen, W.-C.; Huang, B.; Ni, S.-F.; Xiong, Y.; Rogach, A. L.; Wan, Y.; Shen, D.; Yuan, Y.; Chen, J.-X.; Lo, M.-F., et al. (2019). Deep-Red/Near-Infrared Electroluminescence from Single-Component Charge-Transfer Complex via Thermally Activated Delayed Fluorescence Channel. *Adv. Funct. Mater.* 29, 1903112. 10.1002/adfm.201903112.
28. Liang, Q.; Xu, J.; Xue, J.; Qiao, J. (2020). Near-infrared-II thermally activated delayed fluorescence organic light-emitting diodes. *Chem. Commun.* 56, 8988-8991. 10.1039/D0CC02695F.
29. Ye, H.; Kim, D. H.; Chen, X.; Sandanayaka, A. S. D.; Kim, J. U.; Zaborova, E.; Canard, G.; Tsuchiya,

- Y.; Choi, E. Y.; Wu, J. W., et al. (2018). Near-Infrared Electroluminescence and Low Threshold Amplified Spontaneous Emission above 800 nm from a Thermally Activated Delayed Fluorescent Emitter. *Chem. Mater.* 30, 6702-6710. 10.1021/acs.chemmater.8b02247.
30. Madigan, C. F.; Bulović, V. (2003). Solid State Solvation in Amorphous Organic Thin Films. *Phys. Rev. Lett.* 91, 247403.
31. Wang, M.; Huang, Y.-H.; Lin, K.-S.; Yeh, T.-H.; Duan, J.; Ko, T.-Y.; Liu, S.-W.; Wong, K.-T.; Hu, B. (2019). Revealing the Cooperative Relationship between Spin, Energy, and Polarization Parameters toward Developing High-Efficiency Exciplex Light-Emitting Diodes. *Adv. Mater.* 1904114. 10.1002/adma.201904114.
32. Kronik, L.; Kümmel, S. (2018). Dielectric Screening Meets Optimally Tuned Density Functionals. *Adv. Mater.* 30, 1706560. 10.1002/adma.201706560.
33. Shao, Y.; Gan, Z.; Epifanovsky, E.; Gilbert, A. T. B.; Wormit, M.; Kussmann, J.; Lange, A. W.; Behn, A.; Deng, J.; Feng, X., et al. (2015). Advances in molecular quantum chemistry contained in the Q-Chem 4 program package. *Mol. Phys.* 113, 184-215. 10.1080/00268976.2014.952696.
34. Lu, T.; Chen, F. (2012). Multiwfn: A multifunctional wavefunction analyzer. *J. Comput. Chem.* 33, 580-592. 10.1002/jcc.22885.
35. Biswas, S.; Pramanik, A.; Pal, S.; Sarkar, P. (2017). A Theoretical Perspective on the Photovoltaic Performance of S,N-Heteroacenes: An Even–Odd Effect on the Charge Separation Dynamics. *J. Phys. Chem. C* 121, 2574-2587. 10.1021/acs.jpcc.6b11471.
36. Chen, X.-K.; Ravva, M. K.; Li, H.; Ryno, S. M.; Brédas, J.-L. (2016). Effect of Molecular Packing and Charge Delocalization on the Nonradiative Recombination of Charge-Transfer States in Organic Solar Cells. *Adv. Energy Mater.* 6, 1601325. 10.1002/aenm.201601325.
37. Li, C.; Duan, R.; Liang, B.; Han, G.; Wang, S.; Ye, K.; Liu, Y.; Yi, Y.; Wang, Y. (2017). Deep-Red to Near-Infrared Thermally Activated Delayed Fluorescence in Organic Solid Films and Electroluminescent Devices. *Angew. Chem. Int. Ed.* 56, 11525-11529. 10.1002/anie.201706464.
38. Yuan, Y.; Hu, Y.; Zhang, Y.-X.; Lin, J.-D.; Wang, Y.-K.; Jiang, Z.-Q.; Liao, L.-S.; Lee, S.-T. (2017). Over 10% EQE Near-Infrared Electroluminescence Based on a Thermally Activated Delayed Fluorescence Emitter. *Adv. Funct. Mater.* 27, 1700986. 10.1002/adfm.201700986.
39. Kim, D.-H.; D'Aléo, A.; Chen, X.-K.; Sandanayaka, A. D. S.; Yao, D.; Zhao, L.; Komino, T.; Zaborova, E.; Canard, G.; Tsuchiya, Y., et al. (2018). High-efficiency electroluminescence and amplified spontaneous emission from a thermally activated delayed fluorescent near-infrared emitter. *Nat. Photonics* 12, 98-104. 10.1038/s41566-017-0087-y.
40. Furue, R.; Matsuo, K.; Ashikari, Y.; Ooka, H.; Amanokura, N.; Yasuda, T. (2018). Highly Efficient Red–Orange Delayed Fluorescence Emitters Based on Strong  $\pi$ -Accepting Dibenzophenazine and Dibenzoquinoxaline Cores: toward a Rational Pure-Red OLED Design. *Adv. Opt. Mater.* 6, 1701147. 10.1002/adom.201701147.
41. Yang, T.; Liang, B.; Cheng, Z.; Li, C.; Lu, G.; Wang, Y. (2019). Construction of Efficient Deep-Red/Near-Infrared Emitter Based on a Large  $\pi$ -Conjugated Acceptor and Delayed Fluorescence OLEDs with External Quantum Efficiency of over 20%. *J. Phys. Chem. C* 123, 18585-18592. 10.1021/acs.jpcc.9b05875.
42. Li, C.; Duan, L.; Li, H.; Qiu, Y. (2013). Percolative charge transport in a co-evaporated organic molecular mixture. *Org. Electron.* 14, 3312-3317. 10.1016/j.orgel.2013.09.039.
43. Murawski, C.; Leo, K.; Gather, M. C. (2013). Efficiency Roll-Off in Organic Light-Emitting Diodes. *Adv. Mater.* 25, 6801-6827. 10.1002/adma.201301603.
44. Hasan, M.; Shukla, A.; Ahmad, V.; Sobus, J.; Bencheikh, F.; McGregor, S. K. M.; Mamada, M.; Adachi, C.; Lo, S. C.; Namdas, E. B. (2020). Exciton–Exciton Annihilation in Thermally Activated Delayed Fluorescence Emitter. *Adv. Funct. Mater.* 30, 2000580. 10.1002/adfm.202000580.
45. Chai, J.-D.; Head-Gordon, M. (2008). Long-range corrected hybrid density functionals with damped atom–atom dispersion corrections. *Phys. Chem. Chem. Phys.* 10, 6615-6620. 10.1039/B810189B.
46. Frisch, M. J.; Trucks, G. W.; Schlegel, H. B.; Scuseria, G. E.; Robb, M. A.; Cheeseman, J. R.; Scalmani, G.; Barone, V.; Petersson, G. A.; Nakatsuji, H., et al. *Gaussian 16 Rev. C.01*, Wallingford, CT, 2016.